

High-speed 2D and 3D mid-IR imaging with an InGaAs camera

Cite as: APL Photon. 6, 096108 (2021); doi: 10.1063/5.0061661

Submitted: 28 June 2021 • Accepted: 26 August 2021 •

Published Online: 22 September 2021






View Online



Export Citation



CrossMark

Eric O. Potma,¹  David Knez,¹  Martin Ettenberg,² Matthew Wizeman,² Hai Nguyen,² Tom Sudol,² and Dmitry A. Fishman^{1,a)} 

AFFILIATIONS

¹Department of Chemistry, University of California Irvine, Irvine, California 92697, USA

²Princeton Infrared Technologies, Monmouth Junction, New Jersey 08852, USA

^{a)}Author to whom correspondence should be addressed: dmitryf@uci.edu

ABSTRACT

Recent work on mid-infrared (MIR) detection through the process of non-degenerate two-photon absorption (NTA) in semiconducting materials has shown that wide-field MIR imaging can be achieved with standard Si cameras. While this approach enables MIR imaging at high pixel densities, the low nonlinear absorption coefficient of Si prevents fast NTA-based imaging at lower illumination doses. Here, we overcome this limitation by using InGaAs as the photosensor. Taking advantage of the much higher nonlinear absorption coefficient of this direct bandgap semiconductor, we demonstrate high-speed MIR imaging up to 500 fps with under 1 ms exposure per frame, enabling 2D or 3D mapping without pre- or post-processing of the image.

© 2021 Author(s). All article content, except where otherwise noted, is licensed under a Creative Commons Attribution (CC BY) license (<http://creativecommons.org/licenses/by/4.0/>). <https://doi.org/10.1063/5.0061661>

I. INTRODUCTION

The process of non-degenerate two-photon absorption (NTA) forms an attractive strategy for the detection of low energy photons with wide bandgap semiconductors.^{1,2} In NTA, the energy needed for the generation of charge carriers in the semiconductor is determined by the sum of the energies of a long wavelength signal photon and a shorter wavelength gate photon. In particular, NTA has made it possible to detect signals in the mid-infrared (MIR) wavelength range, which roughly spans 3–12 μm , with Si-based detectors.^{3–5} When applied to imaging, detecting MIR light with Si detector technologies offers several advantages compared to the use of low bandgap MIR cameras, including much lower thermal noise and significantly higher pixel densities. For instance, NTA-based imaging with a Si CCD camera has enabled 1.4 Mpx MIR mapping with 100 ms exposure times.⁶ In addition, using a femtosecond gate pulse, axial optical slicing of the 3D MIR image can be achieved, allowing tomographic mapping with contrast based on the sample's MIR spectroscopic transitions.⁷

NTA-based imaging with Si cameras offers a promising route for MIR mapping at high pixel densities. However, Si is an indirect semiconductor, and its nonlinear absorption coefficient is unfavorably low compared to the ones of direct bandgap materials. Another

limitation of Si is its shallow (linear) absorption edge, which translates into a spectral response of the camera that displays a tail on the low energy side, extending from 900 nm to well over 1100 nm. The shallow absorption edge profile limits flexible tuning of gate pulse energies due to one-photon absorption, which renders Si detectors incompatible for NTA-based MIR detection at energies below $\sim 900\text{ cm}^{-1}$. The Urbach tail of direct bandgap semiconductors, on the other hand, generally displays a much steeper profile and would thus enable NTA detection over a more extended MIR tuning range.

In this work, we push the efficiency of NTA-based MIR imaging by selecting a detector based on a direct bandgap semiconducting material. A careful examination of two-photon absorption efficiencies as well as the practical tuning range for MIR detection identifies InGaAs as an ideal candidate for NTA applications. Using an InGaAs camera, we achieve MIR imaging with frame rates that are two orders of magnitude faster than previously shown for Si CCD cameras. We show high-speed 2D and 3D imaging with 1 Mpx frames at 100 fps and 40 kpx frames at 500 fps using exposure times as low as 60 μs per frame. We demonstrate that these new imaging capabilities enable direct *in situ* detection of several mechanical and physio-chemical processes.

II. SEMICONDUCTORS NONLINEARITY SCALING RULE

In the case of linear absorption in semiconducting materials, where one photon excites an electron from the valence to the conduction band, the carrier population in the conduction band scales linearly with incoming optical power. In two-photon absorption, two photons are required to produce a similar transition if the sum of their energies exceeds the bandgap. For degenerate two-photon absorption (DTA), the carrier population scales quadratically with incident optical power. To estimate the efficiency of such a process, an elegant quantum-mechanical model based on Keldysh theory has been developed in the 1980s.⁸⁻¹⁰ Using a two-band model and a second-order perturbation approach, the DTA coefficient can be expressed as follows:^{11,12}

$$\alpha_{DTA} = K\sqrt{E_p} \frac{F_{DTA}(x)}{n^2 E_g^3}, \quad (1)$$

$$F_{DTA} = \frac{(2x-1)^{3/2}}{2^5 x^5} x = \frac{\hbar\omega}{E_g},$$

where E_p is the Kane energy, K is a material independent constant, n is the linear refractive index of the material, and E_g is the semiconductor bandgap energy. This model predicted and later experimentally confirmed the DTA response of a wide variety of narrow and wide direct bandgap semiconductors. Following the logic of Eq. (1), $\alpha_{DTA} n^2$ scales inversely with E_g^3 . Figure 1(a) represents this scaling rule, overlaid with experimental data acquired over several decades.^{1,2,13-16} This graph makes it clear that the results for Si do not follow the general trend. The reason why a two-band model unsuccessfully predicts the transition probability for Si is because it does not capture the effect of the additional phonon mode needed to mediate the transition in momentum space. Several approaches utilizing different transition pathways have been proposed, among which are the “forbidden–forbidden,”¹⁷ “allowed–forbidden,” and

“allowed–allowed” models.^{18,19} However, a more generalized theory is yet to be developed.

The DTA theory can be expanded for the case of non-degenerate two-photon absorption, where the nonlinear absorption coefficient is now expressed as²⁰⁻²²

$$\alpha_{NTA}(x_1, x_2) = K\sqrt{E_p} \frac{F_{NTA}(x_1, x_2)}{n_1 n_2 E_g^3},$$

$$F_{NTA}(x_1, x_2) = \frac{(x_1 + x_2 - 1)^{3/2}}{2^7 x_1^3 x_2^4} (x_1 + x_2)^2, \quad (2)$$

$$x_1 = \frac{\hbar\omega_1}{E_g}, \quad x_2 = \frac{\hbar\omega_2}{E_g}.$$

Here, n_1 and n_2 are the refractive indices of the material at the respective wavelengths of the incident photons. It is useful to relate the nonlinear absorption coefficient defined in (2) to the actual charge carriers generated in the semiconductor, as the number of photo-excited conduction electrons is directly proportional to the signal registered in NTA detection applications. The change in the number of photo-excited electrons N_c in the conduction band as a function of propagation distance z in the material depends on the loss of photon numbers N_1 and N_2 , and can be expressed as

$$\frac{dN_c}{dz} = -\frac{1}{2} \left(\frac{dN_1}{dz} + \frac{dN_2}{dz} \right),$$

$$\frac{dN_1}{dz} = -2\alpha_{NTA}(x_1, x_2) \frac{\hbar\omega_1}{\tau\pi\omega_0^2} N_1 N_2, \quad (3)$$

$$\frac{dN_2}{dz} = -2\alpha_{NTA}(x_2, x_1) \frac{\hbar\omega_2}{\tau\pi\omega_0^2} N_1 N_2,$$

where $\hbar\omega_1$ and $\hbar\omega_2$ are the photon energies, expressed in Joules, τ is the interaction time between the two beams, and $\pi\omega_0^2$ is the illumination area. From Eqs. (2) and (3), it follows that the change in the number of electrons in the conduction band can be written as

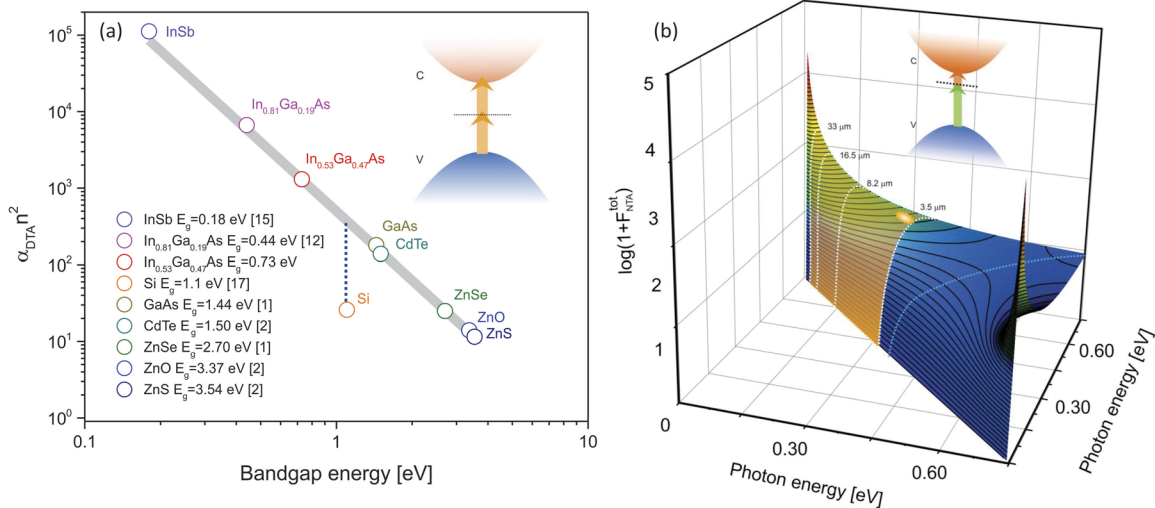


FIG. 1. (a) Scaling rule of the degenerate two-photon absorption coefficient as a function of semiconductor bandgap. (b) F_{NTA}^{tot} function vs two photon energies calculated for lattice matched InGaAs. The light blue curve represents the case of DTA.

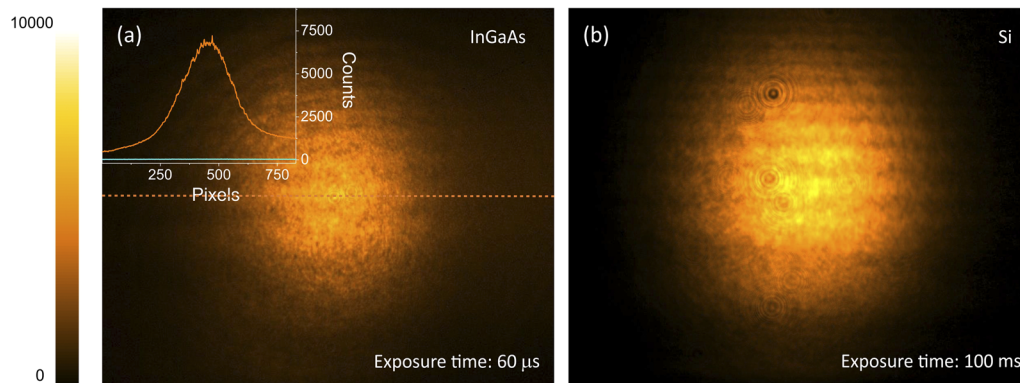


FIG. 2. (a) 4250 nm (~2350 cm⁻¹) single shot detection by an InGaAs camera using 60 μs exposure time. The MIR average power is 130 μW. The inset shows the spatial cross section of the beam profile on the camera chip (orange curve) when both MIR and gate pulses are present. The light blue curve shows the DTA background when only the 1900 nm gate beam is present. (b) 3840 nm (~2600 cm⁻¹) pulse train detection on a Si CCD camera using 100 ms exposure time. The average power is 1 mW.

$$\frac{dN_c}{dz} = \frac{K\sqrt{E_p}}{n_1 n_2 \pi \omega_0^2} \frac{N_1 N_2}{E_g^2} F_{NTA}^{tot},$$

$$F_{NTA}^{tot} = x_2 F_{NTA}(x_1, x_2) + x_1 F_{NTA}(x_2, x_1) \quad (4)$$

$$= \frac{(x_1 + x_2 - 1)^{3/2}}{2^6 x_1^3 x_2^3} (x_1 + x_2)^2.$$

It is interesting to note that the detected NTA signal, which follows from (3), is inversely proportional to E_g^2 in contrast to the E_g^3 scaling of the individual nonlinear coefficients $\alpha_{NTA}(x_1, x_2)$ and $\alpha_{NTA}(x_2, x_1)$. See the [supplementary material](#) for a more detailed derivation of Eq. (3).

The function F_{NTA}^{tot} is symmetric in $\hbar\omega_1$ and $\hbar\omega_2$ and is plotted for the case of InGaAs in Fig. 1(b). Together, Figs. 1(a) and 1(b)

TABLE I. Representative compressed videos of moving targets and live organisms. The frame rate is 30 fps with an exposure time of 1 ms per frame. Multimedia views: <https://doi.org/10.1063/5.0061661.1>; <https://doi.org/10.1063/5.0061661.2>; <https://doi.org/10.1063/5.0061661.3>; <https://doi.org/10.1063/5.0061661.4>; <https://doi.org/10.1063/5.0061661.5>

Real-time recording of target movement		
	Printed target on cellulose acetate film. Movie complementary to Fig. 3	Multimedia view MV1 at 2600 cm ⁻¹ Multimedia view MV2 at 2850 cm ⁻¹ Multimedia view MV3 at 3000 cm ⁻¹
	Printed target on cellulose acetate film. MIR at 4250 nm (~2350 cm ⁻¹)	Multimedia view MV4
	Live recording of <i>Tetramorium caespitum</i> (pavement ant). MIR at 4250 nm (~2350 cm ⁻¹). Chitin exoskeleton of the legs appears semi-transparent at 4250 nm due to low MIR absorption of chitin, a polysaccharide rich in CH ₂ groups	Multimedia view MV5

highlight a few important advantages of InGaAs for broadband MIR detection through NTA. First, the low bandgap of InGaAs gives rise to strong degenerate nonlinear absorption coefficients, yet E_g of the material is large enough to suppress thermally induced transitions relative to thermal effects seen in InSb and HgCdTe. The degenerate case is schematically depicted by the blue line in Fig. 1(b) with a maximum of $\alpha_{DTA} = 135$ cm/GW for photon energies of $\hbar\omega = 0.7E_g$. Second, the non-degenerate two-photon absorption efficiency increases dramatically relative to α_{DTA} when the photon energy ratio disparity $\hbar\omega_1/\hbar\omega_2$ deviates from unity, as predicted by Eq. (3). This enables detection over multiple spectral octaves from 3.5 to >30 μm [Fig. 1(b)] with α_{NTA} approaching tens of MW/cm when $\hbar\omega_{IR}$ is tuned to lower energies.

III. MATERIALS AND METHODS

The experimental setup has been described in previous work.⁷ Particular parameters for the current studies are given in Table 1 of the [supplementary material](#). Two femtosecond pulses, a tunable MIR beam and a fixed near-infrared (NIR) gate beam at 1900 nm (5263 cm^{-1}), are spatially overlapped on the InGaAs camera chip (1280MVCam, Princeton Infrared Technologies, Inc.). The chip is based on the lattice matched $\text{In}_{0.53}\text{Ga}_{0.47}\text{As}$ alloy, which exhibits a steep bandgap absorption edge around 1700 nm (0.73 eV) at room temperature. The quantum efficiency and spectral responsivity curves are presented in Figs. S1 and S2 of the [supplementary](#)

[material](#). The camera enables high-speed imaging utilizing the whole chip of 1280×1024 pixel² (12 μm pixel pitch) up to 100 fps. Faster voltage readout requires reduction of the region of interest, enabling 500 fps for 200×200 pixel² frames. It is important to note that the camera chip is protected by a borosilicate window (thickness 2 mm), which significantly attenuates the MIR radiation (OD = 1.25 at 4200 nm, OD > 5 at 5000 nm, see Fig. S2 of the [supplementary material](#)). The estimated pulse energies are ~ 200 fJ per pixel for the MIR beam (130 μW average power) and ~ 50 fJ per pixel for the 1900 nm gate beam (20 μW average power). The MIR beam is directed to the sample and scattered light is collected by a 100 mm CaF_2 lens, forming an image of the sample onto the camera in a 1:1 fashion. An NTA signal is generated in the InGaAs chip whenever the MIR temporally overlaps with the NIR gate pulse. The current magnification and effective numerical aperture of the imaging lens (NA = 0.015) provides an image with ~ 100 μm resolution, corresponding to ~ 20 pixels on the camera. Better spatial resolution, or a larger field of view, can be achieved by changing the imaging lens.

IV. RESULTS AND DISCUSSION

A. Short exposure time imaging

Figure 2(a) shows an NTA image of the MIR beam at 4250 nm (~ 2350 cm^{-1}) on the InGaAs chip. The high optical nonlinearity of the InGaAs material enables efficient NTA, allowing an exposure



FIG. 3. Chemically selective 2D imaging of a cellulose acetate film. A figure is printed on the film with black ink to generate contrast. If tuned to the resonance of C–H stretching modes, cellulose acetate becomes less transparent, decreasing the contrast between the clear and inked areas of the film. Exposure time: 1 ms. Multimedia views: <https://doi.org/10.1063/5.0061661.1>; <https://doi.org/10.1063/5.0061661.2>; <https://doi.org/10.1063/5.0061661.3>

time of only 60 μs . At such fast exposure times, light contamination from the surrounding is negligible. At the 1 kHz repetition rate of the light source, the inter-pulse separation is 1 ms, which is much longer than the exposure time. Consequently, the signal shown in Fig. 2(a) is caused by a single MIR/gate pulse pair. Similarly, for exposure times less than 1 ms, the NTA signal in illuminated frames is derived from single shots that fall within the exposure time window.

The DTA background can be suppressed when the gate pulse power is lowered relative to the pulse power of the MIR beam, allowing background-free imaging experiments. In Fig. 2(a), the overall signal-to-background ratio is around 20 dB [$10 \log(S_{NTA}/S_{DTA})$], with signal-to-noise of 33 dB [$10 \log(S_{NTA}/\sigma_{DTA})$] or 66 dB [mean root power, $20 \log(S_{NTA}/\sigma_{DTA})$], where σ_{DTA} is the standard deviation of the DTA background signal.

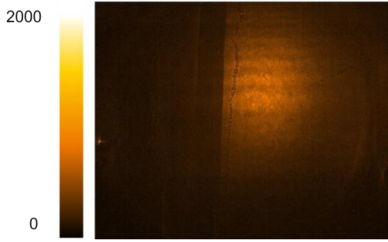
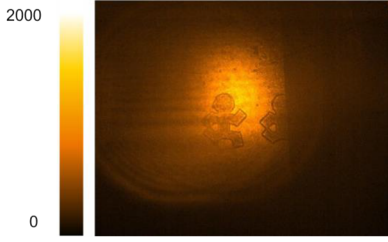
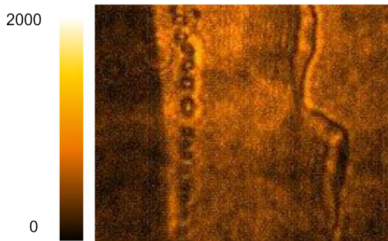
For comparison, Fig. 2(b) shows an NTA image of the same MIR beam collected with a Si CCD camera (Clara, Andor Technologies). The average powers of the MIR and gate beams, as well as the exposure time, are adjusted to achieve roughly the same NTA signal level on the Si camera. Accounting for the differences in illumination conditions, optical properties of protective windows, wavelength-dependent quantum efficiencies of the respective

sensors, and gain settings, we observe that the InGaAs camera exhibits a ~ 110 times higher detection efficiency than its Si counterpart. These observations are in good agreement with Eq. (2), which predicts nonlinear coefficients of 355 cm/GW for InGaAs and 3 cm/GW for Si for the photon energies used in the experiment.

B. Chemically selective MIR videography

The short exposure time enabled by the higher α_{NTA} of InGaAs opens up the possibility of high-speed MIR videography. Table I contains snapshots from MIR videos of moving targets, recorded at 30 fps with 1 ms exposure time per frame. Under these conditions, in each frame, the chip is illuminated on average by a single MIR/gate pulse pair. Among the examples is a structure printed on a $\sim 110 \mu\text{m}$ thick cellulose acetate film, shown in more detail in Fig. 3. One of the advantages of MIR imaging is the capability to generate contrast based on spectroscopic transitions in the material, underlined by the FTIR spectrum of cellulose acetate depicted in Fig. 3(a). The absorption feature in the relevant spectral range corresponds to the C–H stretching vibrational mode. In Fig. 3(b), the MIR beam is tuned to

TABLE II. Time lapse imaging of the mixing process of methanol and D_2O , with frame rates of 30, 100, and 500 fps and an exposure time of 1 ms per frame. Multimedia views: <https://doi.org/10.1063/5.0061661.6>; <https://doi.org/10.1063/5.0061661.7>; <https://doi.org/10.1063/5.0061661.8>

Early mixing dynamics of methanol and D_2O with solvated gas release		
	<p>Methanol and D_2O mixture on a microscope cover slip. MIR at 2600 cm^{-1}</p>	<p>Multimedia view MV6 (30 fps)</p>
	<p>Methanol and D_2O mixture on cellulose acetate film. MIR at 2600 cm^{-1}. Printed structure is clearly seen through methanol</p>	<p>Multimedia view MV7 (100 fps)</p>
	<p>High-speed recoding of solvated gas bubble formation. MIR at 2600 cm^{-1}. Region of interest is $200 \times 200 \text{ px}^2$</p>	<p>Multimedia view MV8 (500 fps)</p>

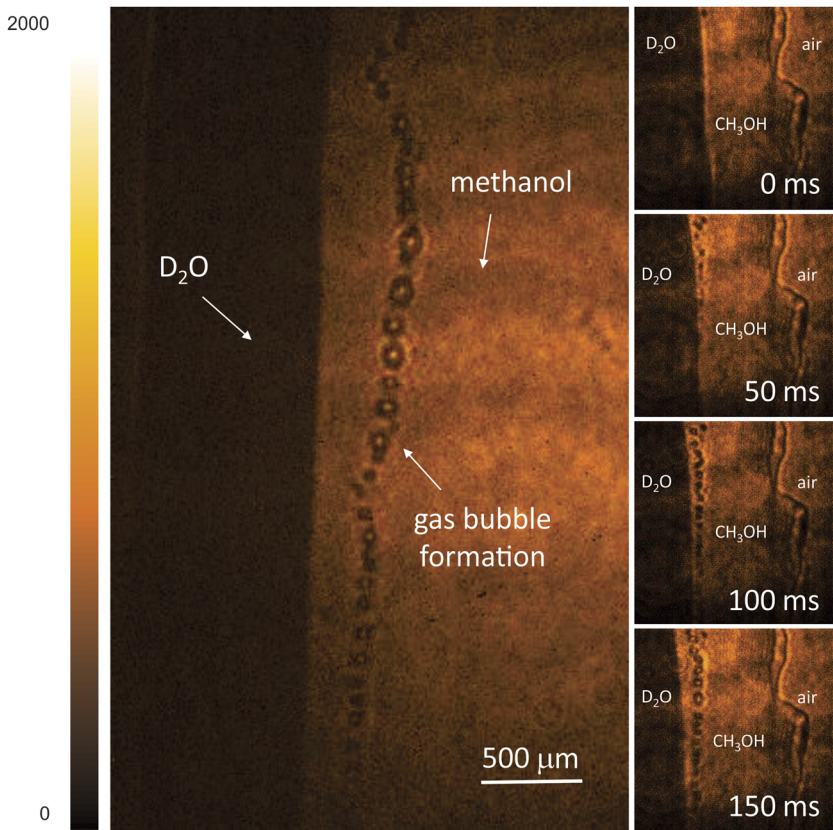


FIG. 4. Snapshots of chemically sensitive 2D time-lapse imaging of the early dynamics of a methanol–D₂O mixture. D₂O appears much darker due to the D–O stretching absorption near 2600 cm⁻¹ (3850 nm), while methanol remains nearly transparent. Bubbles are formed in the first 150 ms. Exposure time: 1 ms.

3000 cm⁻¹ where absorption is significant, reducing the transmission of the MIR light through the material, resulting in poor image contrast. When the MIR beam is tuned off the vibrational resonance, light absorption decreases, enabling more light to pass through the clear part of the film, as illustrated by Figs. 3(c) and 3(d).

Table II contains thumbnails of video recordings of several mixing dynamics experiments based on methanol and D₂O. In these mixing experiments, the active area is visualized in the transmission geometry at acquisition rates of up to 500 fps. In the visible range, both liquids are transparent, hence indistinguishable. However, in

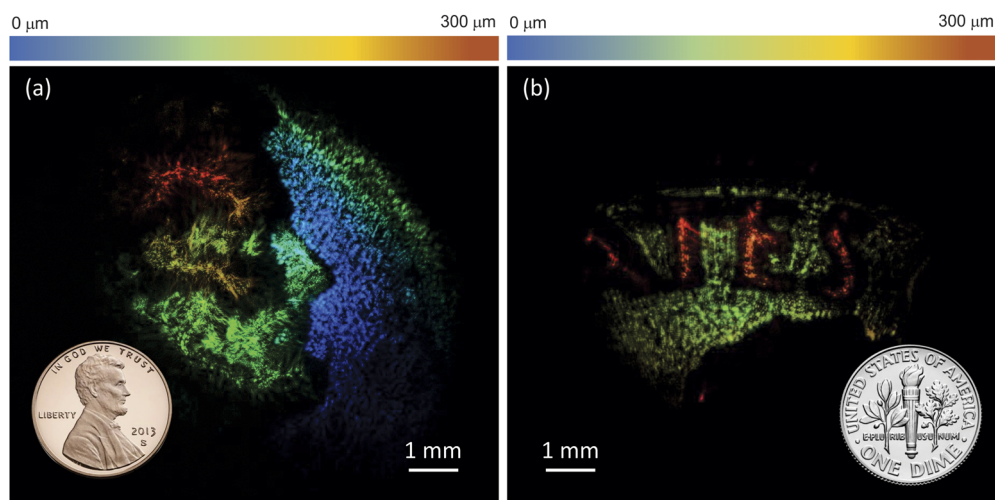


FIG. 5. Tomographic images of the US penny (a) and dime (b) scanned at 4250 nm (2350 cm⁻¹). The total acquisition time for each volumetric scan is 20 ms.

the MIR spectral region, due to the distinct absorption band of D–O stretching vibrations, D₂O appears much darker at 2600 cm⁻¹ (3850 nm), while methanol remains nearly transparent, as shown in Fig. 4. Since mixing and hydrogen bonding between methanol and D₂O molecules is energetically favorable, the process is slightly exothermic.^{23,24} In the early mixing dynamics, the formation of sub-mm bubbles is observed,²⁵ which can possibly be attributed to the mechanism of solvated gas release (N₂, O₂, CO₂) induced by the local increase in temperature near the interfacial regions.^{26,27}

C. High-speed 3D imaging

The use of fs pulses in NTA imaging enables axial optical slicing through temporal gating by the NIR pulse, thus making 3D imaging possible.^{7,28} In this tomographic MIR imaging approach, the depth scan is realized by adjusting the time delay between the MIR and gate pulses at the camera chip. Since the time delay can be scanned rapidly, fs-NTA allows for rapid acquisition of 3D image stacks. When combined with the increase in acquisition speed afforded by the InGaAs camera, truly high-speed 3D imaging in the MIR is within reach. In Fig. 5, we apply this principle to visualize features on the US penny and dime. The axial resolution is determined by the short coherence length of the femtosecond pulses, which in the current work is ~10 μm. Each 2D image frame is acquired in 1 ms, and with 20 images in the 3D data stack, the effective acquisition time is 20 ms. Note that such volumetric imaging rates are more than 50 times higher than previously reported,⁷ emphasizing the drastic improvement of imaging performance with InGaAs cameras.

V. CONCLUSION

In this work, we have significantly advanced the speed of NTA-based MIR imaging by using an InGaAs camera. Compared to Si detectors, the high nonlinear absorption coefficient of InGaAs sensors increases the efficiency of NTA-induced photocurrents by over two orders of magnitude. We have shown that the higher NTA efficiency readily improves the imaging speed by a factor of at least 100 times. At such imaging rates, 2D and 3D visualization of fast dynamic processes at high pixel numbers, which was hitherto inaccessible for MIR imaging, becomes possible. In particular, using the improved imaging capabilities, we have successfully resolved liquid–liquid mixing dynamics of methanol and D₂O on the millisecond timescale, revealing the formation of gas bubbles within a ~100 ms time window. In addition, we have demonstrated the acquisition of 3D images within tens of ms, acquisition speeds that are unprecedented for tomographic mapping in the MIR.

The faster NTA-based MIR imaging capabilities have implications beyond fast videography or 3D imaging. Using chirped broadband MIR pulses, a rapid time-delay scan of the gate pulse would allow for fast spectral sweeping, resulting in the acquisition of hyperspectral data stacks. We anticipate that such data stacks can be recorded at rates exceeding one hyperspectral image per second, hence permitting spectrally resolved imaging of sub-second processes. Whereas the current work uses fs pulses, the high NTA efficiencies demonstrated here open the door for utilization of lower irradiance sources, including commercially available quantum cascade lasers (QCLs). In addition, lower doping levels of indium could shift the In_{1-x}Ga_xAs absorption edge to higher energies according to

$E_g = 0.36 + 0.63x + 0.47x^2$.²⁹ This would render the InGaAs detector suitable for NTA with gate photons derived from Er-doped telecom lasers. Such developments will bring the NTA-based imaging technology into the realm of compact and affordable light sources.

SUPPLEMENTARY MATERIAL

See the [supplementary material](#) for details on the setup and InGaAs camera parameters and derivations of Eqs. (3) and (4).

AUTHORS' CONTRIBUTIONS

E.O.P. and D.A.F. contributed equally to this work.

ACKNOWLEDGMENTS

We acknowledge the National Institutes of Health (Grant No. GM R21-GM141774) and the Air Force STTR AFX20C-TCS01/AFWERX Program (Contract No. F4FBEQ1019A0DP).

DATA AVAILABILITY

The data that support the findings of this study are available from the corresponding author upon reasonable request.

REFERENCES

- D. A. Fishman *et al.*, "Sensitive mid-infrared detection in wide-bandgap semiconductors using extreme non-degenerate two-photon absorption," *Nat. Photonics* **5**(9), 561–565 (2011).
- C. M. Cirloganu *et al.*, "Extremely nondegenerate two-photon absorption in direct-gap semiconductors [invited]," *Opt. Express* **19**(23), 22951–22960 (2011).
- G. Xu *et al.*, "Sensitive infrared photon counting detection by nondegenerate two-photon absorption in Si APD," *IEEE Photonics Technol. Lett.* **31**(24), 1944–1947 (2019).
- N. Cox, D. Hagan, and E. Van Stryland, "Extremely nondegenerate two-photon absorption in silicon (conference presentation)," *Proc. SPIE* **10916**, 1091613 (2019).
- J. Fang *et al.*, "Highly sensitive detection of infrared photons by nondegenerate two-photon absorption under midinfrared pumping," *Phys. Rev. Appl.* **14**(6), 064035 (2020).
- D. Knez *et al.*, "Infrared chemical imaging through non-degenerate two-photon absorption in silicon-based cameras," *Light: Sci. Appl.* **9**(1), 125 (2020).
- E. O. Potma *et al.*, "Rapid chemically selective 3D imaging in the mid-infrared," *Optica* **8**(7), 995–1002 (2021).
- H. D. Jones and H. R. Reiss, "Intense-field effects in solids," *Phys. Rev. B* **16**(6), 2466–2473 (1977).
- L. V. Keldysh, "Ionization in the field of a strong electromagnetic wave," *J. Exp. Theor. Phys.* **20**(5), 1307–1314 (1965).
- B. S. Wherrett, "Scaling rules for multiphoton interband absorption in semiconductors," *J. Opt. Soc. Am. B* **1**(1), 67–72 (1984).
- E. W. Van Stryland *et al.*, "Energy band-gap dependence of two-photon absorption," *Opt. Lett.* **10**(10), 490–492 (1985).
- E. W. Van Stryland *et al.*, "Optical limiting with semiconductors," *J. Opt. Soc. Am. B* **5**(9), 1980–1988 (1988).
- M. Piccardo *et al.*, "Mid-infrared two-photon absorption in an extended-wavelength InGaAs photodetector," *Appl. Phys. Lett.* **112**(4), 041106 (2018).
- H. S. Pattanaik, "Two-photon absorption in bulk semiconductors and quantum well structures and its applications," Ph.D. thesis (CREOL, University of Central Florida, 2015).
- C. M. Cirloganu, "Experimental and theoretical approaches to characterization of electronic nonlinearities in direct-gap semiconductors," Ph.D. thesis (CREOL, University of Central Florida, 2010).

- ¹⁶A. M. Johnston, C. R. Pidgeon, and J. Dempsey, "Frequency dependence of two-photon absorption in InSb and $\text{Hg}_{1-x}\text{Cd}_x\text{Te}$," *Phys. Rev. B* **22**(2), 825–831 (1980).
- ¹⁷M. Dinu, "Dispersion of phonon-assisted nonresonant third-order nonlinearities," *IEEE J. Quantum Electron.* **39**(11), 1498–1503 (2003).
- ¹⁸A. D. Bristow, N. Rotenberg, and H. M. van Driel, "Two-photon absorption and Kerr coefficients of silicon for 850–2200 nm," *Appl. Phys. Lett.* **90**, 191104 (2007).
- ¹⁹H. Garcia and R. Kalyanaraman, "Phonon-assisted two-photon absorption in the presence of a dc-field: The nonlinear Franz-Keldysh effect in indirect gap semiconductors," *J. Phys. B: At., Mol. Opt. Phys.* **39**(12), 2737–2746 (2006).
- ²⁰M. Sheik-Bahae *et al.*, "Measurement of nondegenerate nonlinearities using a two-color Z scan," *Opt. Lett.* **17**(4), 258–260 (1992).
- ²¹D. C. Hutchings and E. W. Van Stryland, "Nondegenerate two-photon absorption in zinc blende semiconductors," *J. Opt. Soc. Am. B* **9**(11), 2065–2074 (1992).
- ²²M. Sheik-Bahae *et al.*, "Dispersion of bound electron nonlinear refraction in solids," *IEEE J. Quantum Electron.* **27**(6), 1296–1309 (1991).
- ²³J. A. Boyne and A. G. Williamson, "Enthalpies of mixture of ethanol and water at 25.degree.C," *J. Chem. Eng. Data* **12**(3), 318 (1967).
- ²⁴D. Peeters and P. Huyskens, "Endothermicity or exothermicity of water/alcohol mixtures," *J. Mol. Struct.* **300**, 539–550 (1993).
- ²⁵G. Rage *et al.*, "Bubbles determine the amount of alcohol in Mezcal," *Sci. Rep.* **10**(1), 11014 (2020).
- ²⁶"Solutions and solubility-behaviour of water," in *Abridged Science for High School Students*, edited by H. Messel (Pergamon, 1966), Chap. 25, pp. 25-1–25-15.
- ²⁷J. C. Millare and B. A. Basilia, "Nanobubbles from ethanol-water mixtures: Generation and solute effects via solvent replacement method," *ChemistrySelect* **3**(32), 9268–9275 (2018).
- ²⁸H. S. Pattanaik *et al.*, "Three-dimensional IR imaging with uncooled GaN photodiodes using nondegenerate two-photon absorption," *Opt. Express* **24**(2), 1196–1205 (2016).
- ²⁹K. H. Goetz *et al.*, "Optical and crystallographic properties and impurity incorporation of $\text{Ga}_x\text{In}_{1-x}\text{As}$ ($0.44 < x < 0.49$) grown by liquid phase epitaxy, vapor phase epitaxy, and metal organic chemical vapor deposition," *J. Appl. Phys.* **54**(8), 4543–4552 (1983).